

ARTICLE

A single emitting layer white OLED based on exciplex interface emission

Received 00th January 20xx,
Accepted 00th January 20xx

DOI: 10.1039/x0xx00000x

www.rsc.org/

E. Angioni,^a M. Chapran,^b K. Ivaniuk,^b N. Kostiv,^b V. Cherpak,^b P. Stakhira,^{b,*} A. Lazauskas,^c S. Tamulevičius,^c D. Volyniuk,^d N. J. Findlay,^a T. Tuttle,^a J. V. Grazulevicius^{d,*} and P. J. Skabara^{a,*}

A new triaryl molecule based on a benzene-benzothiadiazole-benzene core has been applied in a WOLED device. This very simple molecule emits from a combination of emissive states (exciton/electromer/exciplep/electroplex) to give white light with CIE coordinates of (0.38, 0.45) and a colour temperature of 4500K.

Introduction

During the last two decades, the swift development of new and high performing inorganic and organic emissive materials has brought to the market competitive and efficient solid state lighting (SSL) devices. They are predicted to become the next generation of general illumination systems.¹ Inorganic white light emitting diodes (LEDs) are commercially used nowadays for general illumination purposes (*e.g.* automotive lighting, indoor and outdoor lighting).² White organic light emitting diodes (WOLEDs) instead are principally used as low-cost alternatives for back-lights in flat panel displays.³ They present several advantages compared to their inorganic counterparts, such as lower cost, ease of processability and facile tuning of their properties by chemical modifications.^{3, 4} Furthermore, they can be fabricated as flexible panels with wide viewing angles and a superior white colour balance.⁵ White SSL can be achieved using different approaches, but commercially successful methods include: (I) combining a blue (*ca.* 460 nm) LED and a yellow phosphor pumped from the blue light of the LED;⁶⁻⁸ (II) combining a single chip emitting UV light which is absorbed in the LED package by three phosphors (red, green and blue) and re-emitted as a broad spectrum of white light^{9, 10} or (III) three different LED chips, each emitting a different wavelength [red, green and blue (RGB)] in order to simulate the RGB colour model.⁹⁻¹⁵ The design of these configurations is not straightforward and to achieve competitive efficiencies

and luminosity the use of hybrid (inorganic-organic) solutions has been explored.^{11-13, 16} Furthermore, white light produced in this fashion is difficult to fine-tune, in particular when a mixture of several emitters is used.¹⁷ In order to simplify the device architecture, several strategies have been used to fabricate single molecular layer WOLEDs.⁵ Heagy *et al.* employed *N*-aryl-2,3-naphthalimides with low symmetry that exhibited efficient panchromatic emission.^{18, 19} Liu *et al.* observed white solid-state luminescence as well as electroluminescence from the controlled protonation of a molecular blue fluorophore,²⁰ while Chou *et al.* showed white-light emission in a single excited-state-intramolecular-proton-transfer (ESIPT) system by fine-tuning the energetics of the excited state.²¹ White-light emission can also be achieved from intermolecular interactions or from the formation of complexes, *e.g.* excimers or exciplexes.^{17, 22-26} Excimers are possible in single component organic materials due to the resonance interaction of a molecular exciton with a neighbour non-excited molecule,²⁷⁻²⁹ whereas exciplexes can be formed in a bi- or multi-component molecular solid when the formation of bimolecular excited states is facilitated by electron transfer between the donor and acceptor components.^{30, 31} In 2002 Wang and co-workers reported a highly efficient white device based on the exciplex between a boron complex and *N,N'*-di(1-naphthyl)-*N,N'*-diphenylbenzidine (NPB).³² Qiu and co-workers observed exciplex type white-light emission from the interface of a bilayer electroluminescent device consisting of a new electron transport material, anthracene-9,10-diylbis(diphenylphosphine oxide) (DPPA) and *N,N'*-bis(naphthalen-1-yl)-*N,N'*-bis(phenyl)benzidine (NPB)²² as the hole-transporting layer. Recently, Cherpak *et al.* reported a new approach for the fabrication of a WOLED that consists of the combination of the blue phosphorescence emission from the iridium (III) bis[4,6-difluorophenyl]-pyridinato-*N,C2'*-picolate (**Flrpic**) complex and the highly efficient delayed fluorescent emission from the exciplex formed at the interface between the star-shaped hole transporting material tri(9-hexylcarbazol-3-yl)amine and

^a WestCHEM, Department of Pure and Applied Chemistry, University of Strathclyde, Glasgow, G1 1XL, UK. E-mail: peter.skabara@strath.ac.uk

^b Lviv Polytechnic National University, S. Bandera 12, 79013 Lviv, Ukraine.

^c Institute of Materials Science, Kaunas University of Technology, Baršausko str. 59, LT-51423 Kaunas, Lithuania.

^d Department of Polymer Chemistry and Technology, Kaunas University of Technology, Radvilenu Plentas 19, LT-50254 Kaunas, Lithuania.

† Footnotes relating to the title and/or authors should appear here.

Electronic Supplementary Information (ESI) available: [experimental procedures, cyclic voltammetry, spectroscopy data, AFM, modelling, TGA]. See DOI: 10.1039/x0xx00000x

Fig. 1.²⁶ In this work, an OLED based on the new compound dimethyl 4,4'-(benzo[1,2,5]thiadiazole-4,7-diyl)bis(3-methoxybenzoate) (**1**) has been fabricated and its performance studied.

Results and discussion

Synthesis and opto-electronic properties

Compound **1** was synthesised from commercially available 4,7-bis(4,4,5,5-tetramethyl-1,3,2-dioxaborolan-2-yl)benzo[c][1,2,5]thiadiazole *via* Suzuki-Miyaura cross-coupling with methyl 4-iodo-3-methoxybenzoate (**2**) (**Fig. 1a**). In the UV-Vis absorption spectrum of **1** (10^{-5} M in dichloromethane) (**Fig. 1b**) the typical absorption band of the benzothiadiazole (BT) core³⁴⁻³⁶ is blue shifted to 295 nm ($19300\text{ M}^{-1}\text{ cm}^{-1}$) and its vibronic fine structure is visible. In a similar fashion, the less intense band, attributable to the interaction between the peripheral benzene rings and the core (HOMO-LUMO transition, **Table S1**, ESI) is blue shifted and centered at 366 nm ($9500\text{ M}^{-1}\text{ cm}^{-1}$). This is likely due to the non-planarity of **1**, contrary to some planar 4,7-di-substituted benzothiadiazole analogous compounds.³⁶⁻³⁸ From the longest wavelength absorption edge of the UV-Vis absorption spectrum (**Fig. 1**) it was possible to calculate an optical HOMO-LUMO gap of 3.0 eV. Photoluminescence measurements were performed for

a dilute dichloromethane solution of **1** (10^{-6} M) at 300K (excitation at 366 nm) and for a dilute THF solution of **1** (10^{-6} M) at 300 and 77K (excitation at 330 nm) showing emission maxima at 472, 487 and 449 nm, respectively. Furthermore, photoluminescence quantum yields (PLQYs) of *ca.* 50% and *ca.* 6 % were recorded at 300K using an excitation wavelength of 366 nm for the dilute dichloromethane solution of **1** (10^{-6} M) and for the encapsulated powder of **1** (pressed against two glass substrates), respectively. The red shift with decreasing polarity of solvent is likely due to the donor-acceptor character of **1**. In the excited state one expects a large dipole moment due to charge transfer and thus a high sensitivity to solvent polarity. Instead, as the temperature of THF is decreased to 77K, the emission spectrum of **1** is observed from a less relaxed excited state resulted in a shift of the fluorescence maxima to shorter wavelengths.³⁹⁻⁴¹

Cyclic voltammograms were recorded for a dilute solution of **1** in dichloromethane using tetrabutylammonium hexafluorophosphate as the supporting electrolyte. They show a reversible reduction ($-1.99/-1.87\text{ V}$) and three irreversible oxidations (1.36, 1.50, 1.63 V) (**Fig. S1**, ESI). The reduction process can be attributed to the semi-reversible reduction of the BT unit, known to be an electron acceptor,⁴² whereas the anodic waves can be attributed to the oxidation processes likely localised on the methoxy groups as revealed in similar 4,7-bis-substituted BT compounds.^{43, 44} The electrochemical HOMO and LUMO levels were calculated from the onset of the first oxidation wave (-6.0 eV), and reduction wave (-2.9 eV), respectively (the data were referenced to ferrocene, which has a HOMO of -4.8 eV).⁴⁵ The electrochemical HOMO-LUMO gap was therefore determined to be 3.1 eV. With respect to the HOMO energy determined by CV (-6.0 eV), a very close value of 5.9 eV was also calculated as the HOMO level from the photoelectron emission spectrum of the solid state film obtained by vacuum deposition onto an indium tin oxide (ITO) coated glass substrate (**Fig. S2**, ESI). The electrochemical HOMO and LUMO energies were used for the development of the device conception and in the following energy diagrams.^{41, 46}

Morphology and charge transport properties

AFM measurements were performed on vacuum deposited layers of **1** at different deposition rates on glass substrates: (a) $< 0.1\text{ Å s}^{-1}$, (b) 1.5 Å s^{-1} and (c) 10 Å s^{-1} (**Fig. S3**, ESI). They show random oriented pillar/needle-shaped surfaces with the mean height of the peaks (18.41 nm, 20.07 nm and 25.53 nm) and the root mean square roughness (9.38 nm, 10.62 nm and 15.99 nm) increasing with the deposition rate. The surfaces are dominated by peaks with a skewness (*RSk*) of 2.25, 1.63 and 1.29, respectively, and they have a leptokurtic distribution of the morphological features with a kurtosis (*RKu*) of 11.10, 7.58 and 5.20, respectively. The X-ray diffraction patterns recorded on the samples deposited at (a) $< 0.1\text{ Å s}^{-1}$, (b) 1.5 Å s^{-1} and (c) 10 Å s^{-1} (**Fig. S4**, ESI) show a completely amorphous structure for **1**, independent of the deposition rate.

The space-charge-limited current (SCLC) technique was used to evaluate the charge-transporting properties of **1**, as SCLC can

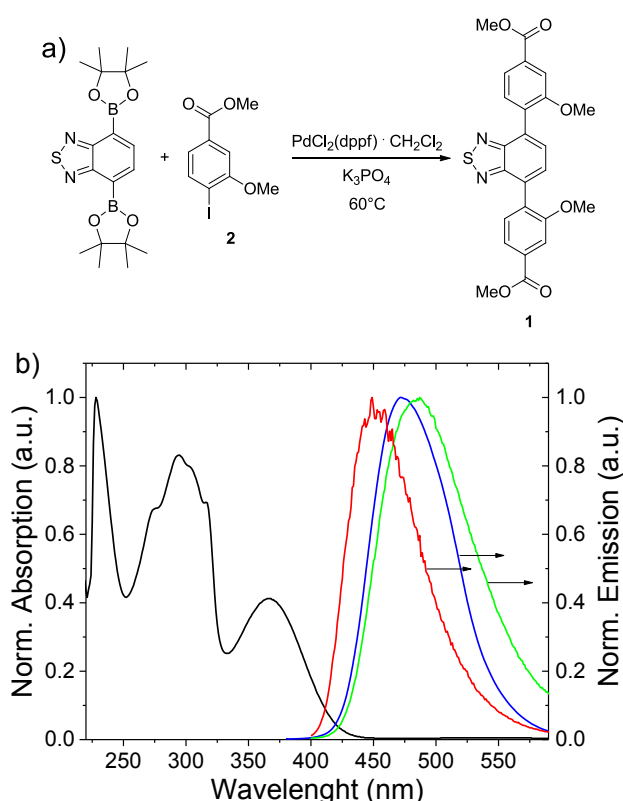


Fig. 1 (a) Synthesis of compound **1** (58% yield). (b) UV-Vis absorption spectrum (black) of a solution of **1** in dichloromethane (10^{-5} M) and the emission spectrum of the solution of **1** in dichloromethane (blue) and tetrahydrofuran (10^{-6} M) at different temperatures (300K, green; 77K, red). The solutions were excited at 366 nm (dichloromethane) and at 330 nm (tetrahydrofuran).

be used to measure the charge carrier mobility in thin films of low molar mass compounds.⁴⁷ Hole-only and electron-only devices were prepared using 4,4',4''-tris[3-methylphenyl(phenyl)amino]triphenylamine (*m*-MTDATA) as the hole-injecting/electron-blocking layer and 1,3,5-tris(*N*-phenylbenzimidazol-2-yl)benzene (TPBi) as the electron-injecting/hole-blocking layer. The two devices were fabricated by successive deposition onto a pre-cleaned indium tin oxide (ITO) coated glass substrate under a vacuum of 10^{-6} Torr, with architectures of: ITO/*m*-MTDATA(20 nm)/**1**(60 nm)/*m*-MTDATA(20 nm)/Al(60 nm) (hole-only) and ITO/TPBi(20 nm)/**1**(60 nm)/TPBi(20 nm)/Ca(10 nm)/Al(60 nm) (electron only). The hole mobility of **1** ($7.6 \times 10^{-7} \text{ cm}^2 \text{ V}^{-1} \text{ s}^{-1}$ at $9.6 \times 10^5 \text{ V cm}^{-1}$) has a higher value than the electron mobility ($1.7 \times 10^{-7} \text{ cm}^2 \text{ V}^{-1} \text{ s}^{-1}$ at $9.6 \times 10^5 \text{ V cm}^{-1}$; Fig. S5, ESI). The fitted parameters μ_0 and γ are $2.6 \times 10^{-8} \text{ cm}^2 \text{ V}^{-1} \text{ s}^{-1}$ and $3.4 \times 10^{-3} \text{ cm V}^{-1}$, and $2.8 \times 10^{-9} \text{ cm}^2 \text{ V}^{-1} \text{ s}^{-1}$ and $4.2 \times 10^{-3} \text{ cm V}^{-1}$ for holes and electrons, respectively (Fig. S6, ESI). Despite the low charge mobility, **1** can be used successfully for the preparation of emitting layers, due to the nano-scale thicknesses required for the OLED fabrication.⁴⁸

Device fabrication and exciplex emission

An electroluminescent device based on **1** was fabricated. Due to the morphology, the low mobility and the energetically deep HOMO level of **1**, *N,N'*-bis(3-methylphenyl)-*N,N'*-diphenylbenzidine (TPD) was used as hole-transporting material to promote a cross-interaction between the excess of electrons from the LUMO of **1** and the excess of holes from the HOMO of TPD with the aim of inducing the formation of a dimeric excited state (e.g. exciplex). 2,9-Dimethyl-4,7-diphenyl-1,10-phenanthroline (BCP) was used as an electron-transporting/hole-blocking layer in order to increase the injection of electrons from the calcium anode and to balance the amount of electrons and holes that combine in the emissive layer. Additionally, to promote hole and electron mobility, CuI was used as a hole-injecting material.

The electroluminescent device (Fig. S7, ESI) was fabricated by successive deposition onto a pre-cleaned indium tin oxide (ITO) coated glass substrate under a vacuum of 10^{-5} Torr using specific deposition rates for the different layers: ITO/CuI (8 nm, 0.1 nm s^{-1})/TPD (10 nm, 0.2 nm s^{-1})/**1** (100 nm, 1 nm s^{-1})/BCP (30 nm, 0.2 nm s^{-1})/Ca (7 nm, 0.1 nm s^{-1})/Al (100 nm, 0.1 nm s^{-1}). The active area of the obtained device was 6 mm^2 and additional passivation was not applied. The fast deposition rate (10 Å s^{-1}) was adopted in the device fabrication process in order to facilitate the creation of an interaction with the adjacent layers. The electroluminescence (EL) spectrum of the device recorded with an applied voltage of 15 V (Fig. 2a) reveals four superimposed different emission bands. The origins of these bands are shown in Fig. S8. The higher energy emission band (494 nm) is characteristic of the pure fluorescence emission of **1**. This is supported by the luminescence decay time measurements of the spin coated film of **1** (at 488 nm, ca. 10^{-2} M in THF) being on a nanosecond scale (Fig. 2b) and from the single emission band centred at 490 nm in its photoluminescence spectrum (Fig. 2a).⁴⁹ The

main band at ca. 580 nm originates from the exciplex at the interface between **1** and the hole-transporting material TPD. In fact, the luminescence decay time measurements (at 580 nm) of the composite layer prepared by spin coating a solution of **1** and TPD (ca. 0.01M in THF) onto a clean quartz substrate shows a combination of 17 ns (41%) and 61 ns (59%) decay times (Fig. 2b), due to the presence of both the exciton fluorescence emission and the exciplex emission at the interface between TPD and **1**.^{26, 49, 50} When a direct bias is applied, due to high energy barriers between TPD and **1** ($\text{HOMO}^{\text{TPD}} - \text{HOMO}^{\text{1}} = 0.5 \text{ eV}$; $\text{LUMO}^{\text{TPD}} - \text{LUMO}^{\text{1}} = 0.6 \text{ eV}$), electrons and holes accumulate at the interface between the two layers and, due to non-planar conformations, the electronic overlap of donor (TPD) and acceptor (**1**) molecules is efficient for exciplex formation at the interface. In fact, the twisted nature of **1** makes self-stacking less likely, increasing the probability of a hetero-interaction with an adjoining molecule. The long-wavelength shoulder at 635 nm in the EL spectra can be assigned to the typical (classic) electroplex interaction that is associated with the exciplex emission.^{49, 51} The band at ca. 520 nm can be attributed to an electromer interaction, that appears upon the injection of electrons and holes under an electric field effect in **1**.^{52, 53} The formation of an electromer is

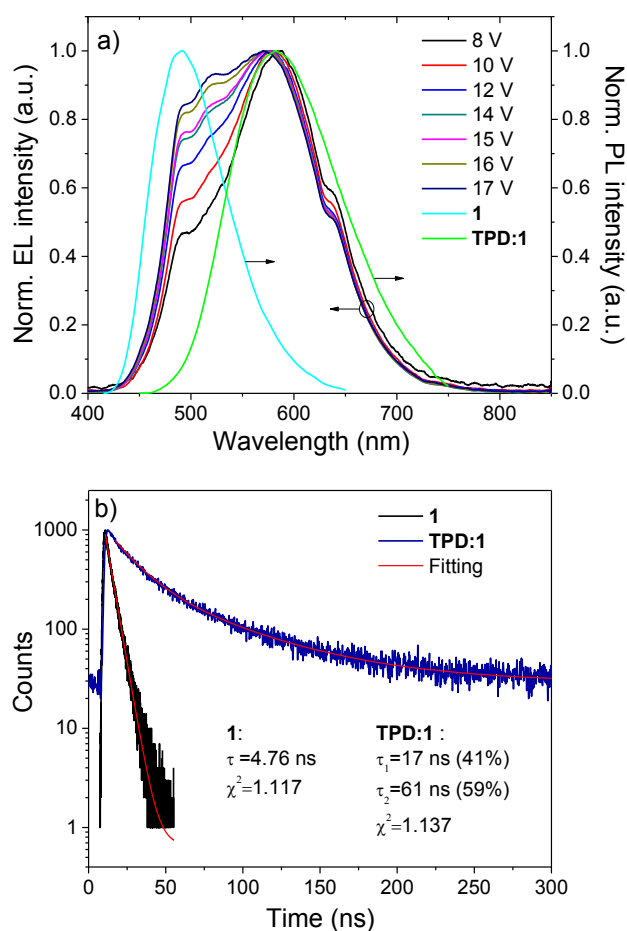


Fig. 2 (a) Electroluminescence spectra of the OLED at selected applied voltages and photoluminescence spectra of the thin films of **1** and of the mixture of TPD with **1** (1:1

w/w). (b) Decay fluorescence plots measured for the thin films of **1** (at 488 nm) and of the mixture of **TPD** with **1** (at 580 nm).

observed when a pair of trapped carriers recombines under an electronic interaction and its emission is red-shifted with respect to fluorescence.⁵¹ Therefore, the white emission of the device originates from the combination of the exciplex/electroplex emission at the interface between **TPD** and **1** and from the exciton/electromer emission of **1**. This is possibly due to the thickness of the emissive layer (100 nm) that permits emission from all the excited states simultaneously. The EL spectra at different applied voltages were recorded (Fig. 2a) and they reveal four different emission bands, with relative intensities that depend on the applied voltage. The maxima of the higher energy emission band (494 nm) and of the electromer emission (520 nm) stay constant with increasing applied voltage, whilst the relative intensities increase. The main emission maximum is blue-shifted from 588 to 570 nm when the applied voltage is increased from 8 to 17 V. Conversely, both the position and the intensity of the shoulder at 635 nm remains effectively unchanged at the different applied voltages. Despite these behaviours, the colour quality of the device is maintained at all applied voltages. The CIE coordinates change only slightly from (0.42, 0.44) when the EL is recorded at 8 V to (0.37, 0.44) at 17 V (Fig. S9 and Table S2, ESI), due mainly to the increased relative intensity of the EL and of the electromer transition of **1**. However, at applied voltages higher than 15 V, the device tends to quickly degrade and the characteristics recorded are not maintained. For this reason the following characteristics of the device were recorded up to a maximum applied voltage of 15 V.

The current density–voltage characteristics and luminance–voltage characteristics (Table S3–S4, ESI) indicate an OLED turn on voltage of 5.8 V, which corresponds to an electroluminescence of 1.4 cd m⁻². The device exhibits a maximum current efficiency of 6.5 cd A⁻¹ and a maximum brightness of 5219 cd m⁻² (at 15 V) (Fig. S10–S12, ESI). At maximum brightness an external quantum efficiency of 2.39% and power efficiency of 2.60 lm W⁻¹ were recorded. The white light emitted from the device at 15 V has Commission Internationale d’Eclairage (CIE 1931) coordinates of (0.38, 0.45) (Fig. S9), with a colour temperature of 4500K; values similar to those of commercial fluorescent tubes.^{13, 54, 55} The relatively low brightness and current efficiency of the single-layer OLED can be explained by the presence of electroplex emission that naturally results in the decrease of OLED efficiency.⁵⁶ On the other hand, the presence of the electroplex-type excited states makes it possible to expand the EL spectrum towards the red region and to obtain a white OLED with a simplified structure.⁵⁶

Computational results

To explain the PL and EL spectra observed experimentally, quantum chemical calculations were performed for **1**, **TPD** and **1:TPD** complexes using density functional theory (DFT) and its time resolved counterpart (TD-DFT).^{57, 58} In order to choose the

most suitable level of theory capable of simulating the vertical transitions associated with the absorption spectra, a benchmark was performed (Table S5, ESI) and, as a result, the PBE0/6-311G(d,p) level of theory was used for all the calculations. Initially eight different geometric isomers of the **TPD:1** complexes (a–h) were optimised (Fig. S13, ESI), with isomer **a** showing the total energy minima and hence was chosen as the starting geometry for the following calculation (Table S6, ESI). The ground state geometries for **1**, **TPD** and the complex **TPD:1** were optimised (Fig. S13–14, ESI) and analysis of the vibrational frequencies revealed the location of the

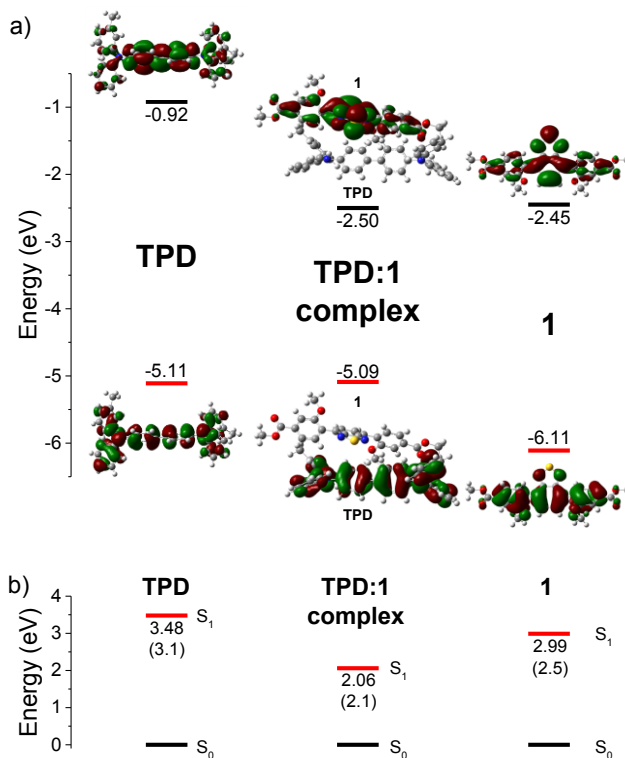


Fig. 3 a) Kohn-Sham molecular orbital diagram and orbital graphical representations (HOMO and LUMO) of **TPD**, **1** and of the complex **TPD:1** calculated at the PBE0/6-311G(d,p) level of theory (isosurface 0.02). b) First singlet excited state energies calculated at the PBE0/6-311G(d,p) level of theory for **TPD**, **1** and for the complex **TPD:1**; the figures in parentheses are the energy levels determined experimentally.

sought-for energy minimum. The HOMO and LUMO orbitals are widely delocalised on the π backbone for **1** and **TPD**, with their energy gaps agreeing qualitatively with the experimental data (Fig. 3a). The **TPD:1** complex shows a LUMO localised on **1** and a HOMO localised on the **TPD** molecule. The reorganisation energies for electrons (λ_e) and holes (λ_h) were calculated theoretically⁵⁹ for **1**. The values obtained for λ_e = 0.425 eV and λ_h = 0.384 eV agree qualitatively with the experimental observations, as the reorganisation energy for the electrons is slightly higher than the corresponding value for holes. Note that the lower the λ value, the higher the charge-transport rate.⁵⁹ The first 20 singlet vertical transitions were calculated in the vacuum (Table S1, S7, S8, ESI) using the TD-DFT/PBE0/6-311G(d,p) level of theory. The energies of the first singlet excited state (S₁) of **1**, **TPD** and of the **TPD:1**

complex are reported in **Fig. 3b**. They agree qualitatively, by the levels of relative disposition, with the experimental PL emission maxima of thin films of the mixture of **TPD:1** and compound **1**, and from the literature data for the film of **TPD**.⁶⁰ The recombination process of an electron–hole pair with the electron located on the LUMO of **1** and the hole located on the HOMO of **TPD** should then be responsible for the EL maximum at ca. 580 nm for the device and explains the exciplex nature of this transition. Here the exciplex is considered as an excited state complex that is formed by an electronically excited state donor molecule (or acceptor) with a complementary acceptor molecule (or donor) in their ground state.⁶¹

Conclusions

A WOLED containing the small and simple organic molecule **1** was fabricated. The resulting electroluminescence was shown to be a combination of the exciton/electromer emission of **1** and of the exciplex/electroplex emission at the heterojunction between **1** and **TPD**. The device has a maximum current efficiency of 6.5 cd/A, a maximum brightness of 5219 cd/m² and good colour quality with C.I.E. 1931 coordinates (0.38, 0.45) at 15 V and a colour temperature of 4500K.

Acknowledgements

The authors would like to thank the UK Engineering and Physical Sciences Research Council (Grant No: EP/I012591/1), the European Commission (Marie Curie Action of FP7, Grant No: PIRSES-GA-2013-612670), the University of Strathclyde, the Lviv Polytechnic National University and the Kaunas University of Technology for the financial support. We thank the EPSRC UK National mass spectrometry facility for the HRMS measurements. PJS thanks the Royal Society for a Wolfson Research Merit Award.

References

1. Y. Takei, *Sci. Technol. Trends–Quarterly Rev.*, 2009, **32**, 59.
2. M. Bessho and K. Shimizu, *Electron. Comm. Jpn.*, 2012, **95**, 1.
3. J. Kalinowski, V. Fattori, M. Cocchi and J. A. G. Williams, *Coord. Chem. Rev.*, 2011, **255**, 2401.
4. J. Roncali, *Macromol. Rapid Commun.*, 2007, **28**, 1761.
5. S. Mukherjee and P. Thilagar, *Dyes Pigm.*, 2014, **110**, 2.
6. K. Bando, K. Sakano, Y. Noguchi and Y. Shimizu, *J. Light & Vis. Env.*, 1998, **22**, 2.
7. R.-J. Xie, N. Hirotsaki, M. Mitomo, Y. Yamamoto, T. Suehiro and K. Sakuma, *J. Phys. Chem. B*, 2004, **108**, 12027.
8. R.-J. Xie, N. Hirotsaki, K. Sakuma, Y. Yamamoto and M. Mitomo, *Appl. Phys. Lett.*, 2004, **84**, 5404.
9. J. K. Sheu, S. J. Chang, C. H. Kuo, Y. K. Su, L. W. Wu, Y. C. Lin, W. C. Lai, J. M. Tsai, G. C. Chi and R. K. Wu, *IEEE Photon. Technol. Lett.*, 2003, **15**, 18.
10. W.-J. Yang, L. Luo, T.-M. Chen and N.-S. Wang, *Chem. Mater.*, 2005, **17**, 3883.
11. K. T. Kamtekar, A. P. Monkman and M. R. Bryce, *Adv. Mater.*, 2010, **22**, 572.
12. C. Tang, X.-D. Liu, F. Liu, X.-L. Wang, H. Xu and W. Huang, *Macromol. Chem. Phys.*, 2013, **214**, 314.
13. M. C. Gather, A. Köhnen and K. Meerholz, *Adv. Mater.*, 2011, **23**, 233.
14. N. Thejo Kalyani and S. J. Dhoble, *Renew. Sust. Energ. Rev.*, 2012, **16**, 2696.
15. I. Moreno and U. Contreras, *Opt. Express*, 2007, **15**, 3607.
16. N. J. Findlay, J. Bruckbauer, A. R. Inigo, B. Breig, S. Arumugam, D. J. Wallis, R. W. Martin and P. J. Skabara, *Adv. Mater.*, 2014, **26**, 7290.
17. G. Giro, M. Cocchi, J. Kalinowski, P. Di Marco and V. Fattori, *Chem. Phys. Lett.*, 2000, **318**, 137.
18. P. Nandhikonda and M. D. Heagy, *Chem. Commun.*, 2010, **46**, 8002.
19. P. Nandhikonda and M. D. Heagy, *Org. Lett.*, 2010, **12**, 4796.
20. D. Liu, Z. Zhang, H. Zhang and Y. Wang, *Chem. Commun.*, 2013, **49**, 10001.
21. K.-C. Tang, M.-J. Chang, T.-Y. Lin, H.-A. Pan, T.-C. Fang, K.-Y. Chen, W.-Y. Hung, Y.-H. Hsu and P.-T. Chou, *J. Am. Chem. Soc.*, 2011, **133**, 17738.
22. Y. Zhao, L. Duan, X. Zhang, D. Zhang, J. Qiao, G. Dong, L. Wang and Y. Qiu, *RSC Adv.*, 2013, **3**, 21453.
23. J. Karpiuk, E. Karolak and J. Nowacki, *Phys. Chem. Chem. Phys.*, 2010, **12**, 8804.
24. V. Jankus, P. Data, D. Graves, C. McGuinness, J. Santos, M. R. Bryce, F. B. Dias and A. P. Monkman, *Adv. Funct. Mater.*, 2014, **24**, 6178.
25. T. Ishisone, S. Seo, Y. Nonaka, T. Kawata and N. Ohsawa, *J. Soc. Inf. Display*, 2014, **22**, 404.
26. V. Cherpak, P. Stakhira, B. Minaev, G. Baryshnikov, E. Stromylo, I. Helzhynskyy, M. Chapran, D. Volyniuk, Z. Hotra, A. Dabulienė, A. Tomkeviciene, L. Voznyak and J. V. Grazulevicius, *ACS Appl. Mater. Interfaces*, 2015, **7**, 1219.
27. D. Thirion, M. Romain, J. I. Rault-Berthelot and C. Poriel, *J. Mater. Chem.*, 2012, **22**, 7149.

28. J.-Y. Hu, Y.-J. Pu, Y. Yamashita, F. Satoh, S. Kawata, H. Katagiri, H. Sasabe and J. Kido, *J. Mater. Chem. C*, 2013, **1**, 3871.
29. J.-Y. Hu, Y.-J. Pu, G. Nakata, S. Kawata, H. Sasabe and J. Kido, *Chem. Commun.*, 2012, **48**, 8434.
30. M. Sharnoff, *J. Lumin.*, 1971, **4**, 69.
31. S. Yang and M. Jiang, *Chem. Phys. Lett.*, 2009, **484**, 54.
32. Y. Liu, J. Guo, H. Zhang and Y. Wang, *Angew. Chem. Int. Ed.*, 2002, **41**, 182.
33. D. Rankine, A. Avellaneda, M. R. Hill, C. J. Doonan and C. J. Sumby, *Chem. Commun.*, 2012, **48**, 10328.
34. J.-M. Raimundo, P. Blanchard, H. Brisset, S. Akoudad and J. Roncali, *Chem. Commun.*, 2000, 939.
35. B. A. D. Neto, A. A. M. Lapis, E. N. da Silva Júnior and J. Dupont, *Eur. J. Org. Chem.*, 2013, **2013**, 228.
36. S.-i. Kato, T. Matsumoto, T. Ishi-i, T. Thiemann, M. Shigeiwa, H. Gorohmaru, S. Maeda, Y. Yamashita and S. Mataka, *Chem. Commun.*, 2004, 2342.
37. M. Akhtaruzzaman, N. Kamata, J.-i. Nishida, S. Ando, H. Tada, M. Tomura and Y. Yamashita, *Chem. Commun.*, 2005, 3183.
38. D. Aldakov, M. A. Palacios and P. Anzenbacher, *Chem. Mater.*, 2005, **17**, 5238.
39. W. Rettig, *Angew. Chem. Int. Ed.*, 1986, **25**, 971.
40. J. R. Lakowicz and A. Balter, *Photochem. Photobiol.*, 1982, **36**, 125.
41. G. Weber and F. J. Farris, *Biochemistry*, 1979, **18**, 3075.
42. P. Ledwon, N. Thomson, E. Angioni, N. J. Findlay, P. J. Skabara and W. Domagala, *RSC Adv.*, 2015, **5**, 77303.
43. K. M. Omer, S.-Y. Ku, K.-T. Wong and A. J. Bard, *J. Am. Chem. Soc.*, 2009, **131**, 10733.
44. G. M. Saltan, H. Dinçalp, M. Kiran, C. Zafer and S. Ç. Erbaş, *Mater. Chem. Phys.*, 2015, **163**, 387.
45. J. L. Bredas, R. Silbey, D. S. Boudreaux and R. R. Chance, *J. Am. Chem. Soc.*, 1983, **105**, 6555.
46. J. Sworakowski and J. Ulanski, *Annu. Rep. Prog. Chem., Sect. C: Phys. Chem.*, 2003, **99**, 87.
47. J. C. Blakesley, F. A. Castro, W. Kylberg, G. F. A. Dibb, C. Arantes, R. Valaski, M. Cremona, J. S. Kim and J.-S. Kim, *Org. Electron.*, 2014, **15**, 1263.
48. S. R. Tseng, Y. S. Chen, H. F. Meng, H. C. Lai, C. H. Yeh, S. F. Horng, H. H. Liao and C. S. Hsu, *Synth. Met.*, 2009, **159**, 137.
49. J. Kalinowski, M. Cocchi, D. Virgili, V. Fattori and J. A. G. Williams, *Adv. Mater.*, 2007, **19**, 4000.
50. Y.-H. Lee, T.-C. Wu, C.-W. Liaw, T.-C. Wen, S.-W. Feng, J.-J. Lee, Y.-T. Wu and T.-F. Guo, *Org. Electron.*, 2013, **14**, 1064.
51. J. Kalinowski, *Mater. Sci.-Poland*, 2009, **27**, 735.
52. S. Kwon, K.-R. Wee, C. Pac and S. O. Kang, *Org. Electron.*, 2012, **13**, 645.
53. J. Kalinowski, G. Giro, M. Cocchi, V. Fattori and P. Di Marco, *Appl. Phys. Lett.*, 2000, **76**, 2352.
54. G. M. Farinola and R. Ragni, *Chem. Soc. Rev.*, 2011, **40**, 3467.
55. Q. Wang and D. Ma, *Chem. Soc. Rev.*, 2010, **39**, 2387.
56. G. M. Farinola and R. Ragni, *Chem. Soc. Rev.*, **2011**, *40*, 3467.
57. R. Improta, V. Barone, G. Scalmani and M. J. Frisch, *J. Chem. Phys.*, 2006, **125**, 054103.
58. F. Furche and R. Ahlrichs, *J. Chem. Phys.*, 2002, **117**, 7433.
59. L.-Y. Zou, A.-M. Ren, J.-K. Feng and X.-Q. Ran, *J. Phys. Org. Chem.*, 2009, **22**, 1104.
60. H. Mattoussi, H. Murata, C. D. Merritt, Y. Iizumi, J. Kido and Z. H. Kafafi, *J. Appl. Phys.*, 1999, **86**, 2642.
61. C.-C. Yang, C.-J. Hsu, P.-T. Chou, H. C. Cheng, Y. O. Su and M.-k. Leung, *J. Phys. Chem. B*, 2010, **114**, 756.

Electronic Supplementary Information Section

A single emitting layer white OLED based on exciplex interface emission

Enrico Angioni, Marian Chapran, Khrystyna Ivaniuk, Nataliya Kostiv, Vladyslav Cherpak, Pavlo Stakhira, Algirdas Lazauskas, Sigitas Tamulevičius, Dmytro Volyniuk, Neil J. Findlay, Tell Tuttle, Juozas V. Grazulevicius,* Peter J. Skabara**

General Experimental

All reactions were performed using vacuum Schlenk lines, in an inert atmosphere of nitrogen. Dry solvents were obtained from a solvent purification system (SPS 400 from Innovative Technologies) using alumina as the drying agent. The compounds 4-iodo-3-hydroxybenzoic acid,¹ methyl 4-iodo-3-hydroxybenzoate,¹ methyl 4-iodo-3-methoxybenzoate (**2**)¹ were synthesised and analysed using literature procedures. All the other reagents were purchased from Sigma Aldrich or Alfa Aesar and used without further purifications. ¹H and ¹³C NMR spectra were recorded on a Bruker Avance DPX400 apparatus at 400.1 and 100.6 MHz. Chemical shifts are given in ppm; all *J* values are in Hz. MS LDI-TOF spectra were run on a Shimadzu Axima-CFR spectrometer (mass range 1-150000 Da). The high resolution mass measurements were performed on the Thermo Scientific LTQ ORBITRAP XL instrument, using the nano-electrospray ionisation (nano-ESI) technique. Thermogravimetric analysis (TGA) was performed using a Perkin-Elmer Thermogravimetric Analyser TGA7 under a constant flow of argon. Melting points were taken using a TA instruments DSC QC1000 Differential Scanning Calorimeter. Cyclic voltammetry (CV) measurements were performed on a CH Instruments 660A electrochemical workstation with *i*R compensation using anhydrous dichloromethane as the solvent. The electrodes were glassy carbon, platinum wire and silver wire as the working, counter and reference electrodes, respectively. All solutions were degassed (Ar) and contained the substrate in concentrations of *ca.* 10⁻⁴ M, together with n-Bu₄NPF₆ (0.1M) as the supporting electrolyte. All measurements are referenced against the E_{1/2} of the F_c/F_c⁺ redox couple. Absorption spectra were recorded on a Shimadzu UV 2700 instrument. Photoluminescence measurements were recorded using a Perkin-Elmer LS 50 B fluorescence spectrometer in a quartz cuvette (path length 10 mm). Absolute photoluminescence quantum yield measurements were measured according to the de Mello² method by using a calibrated integrating sphere attached to an USB 2000 spectrometer and Gooch & Housego spectrometer. Excitation light was chosen from a Quartz Tungsten

Halogen lamp by using a Gooch & Housego spectrometer and the emission light was collected by Ocean optics USB 2000 spectrometer. Measurements were performed in air. The ionisation potential of **1** was measured by the electron photoemission method in air.³ The samples were fabricated by means of vacuum deposition of **1** onto an indium tin oxide (ITO) coated glass substrate. The experimental setup consists of the deep-UV deuterium light source ASBN-D130-CM, the CM110 1/8m monochromator, and the 6517B Keithley electrometer. Characteristics of the current density–voltage and luminance–voltage dependences were measured with a semiconductor parameter analyser (HP 4145A) using it in air without passivation immediately after fabrication of the device. The measurement of brightness was performed using a calibrated photodiode.⁴ Calibration of the photodetector was carried out using a radiometer RTN 20 (accuracy $\pm 2\%$). The photodiode was placed in front of the OLED in a dark room and the calibration was performed according to the method described earlier.⁵ The external quantum efficiency (EQE) values were determined using the equations given in reference 6. The OLED electroluminescence and photoluminescence (PL) spectra of the solid films were recorded with an Ocean Optics USB2000 spectrometer. For the spectral studies the single layers of **1** as well as the **1:TPD** composite layer were prepared by thermovacuum deposition at 10^{-6} Torr onto clean quartz substrates or spin coating *ca.* 2M solutions of **1** as well as **1/TPD** onto clean quartz substrates. Luminescence spectra and luminescence decay curves of the layers were recorded with an Edinburgh Instruments FLS980 spectrometer at 77 K and room temperature using a low repetition rate μ F920H Xenon Flashlamp as the excitation source. The emission was measured twice: immediately after excitation and with a delay after the pulse was turned off (the delay time was set to be *ca.* 30 μ s). Chromaticity coordinates (CIE 1931) and correlated colour temperatures (CCT) are calculated from the response-corrected spectra. X-ray diffraction measurements at grazing incidence (XRDGI) were performed using a D8 Discover diffractometer (Bruker) with Cu K α ($\lambda = 1.54$ Å) X-ray source. Parallel beam geometry with a 60 mm Göbel mirror (X-ray mirror on a high precision parabolic surface) was used. This configuration enables transforming the divergent incident X-ray beam from a line focus of the X-ray tube into a parallel beam that is free of K β radiation. The primary side also had a Soller slit with an axial divergence of 2.5°. The secondary side had a LYNXEYE (0D mode) detector with an opening angle of 1.275° and slit opening of 9.5 mm. The sample stage was a Centric Eulerian cradle mounted to a horizontal D8 Discover with a vacuum chuck (sample holder) fixed on the top of the stage. X-ray generator voltage and current was 40.0 kV and 40 mA, respectively. XRDGI scans were performed in the range of 5.0–135.0° with a step size of 0.066°, time per step of 0.2 s

and auto-repeat function enabled. The resultant diffractograms were processed with the software DIFFRAC.EVA. AFM experiments were carried out in air at room temperature using a NanoWizardIII atomic force microscope (JPK Instruments), while data were analysed using SurfaceXplorer and JPKSPM Data Processing software. AFM images were collected using a V-shaped silicon cantilever (spring constant of 3 N/m, tip curvature radius of 10.0 nm and the cone angle of 20°) operating in contact mode. The space-charge-limited current (SCLC) measurements were adopted for the estimation of charge drift mobility of **1**. Hole-only and electron-only devices were fabricated as described in the paper. The current density vs. voltage characteristics of the hole-only and electron-only devices were recorded and fitted using the Mott-Gurney law:⁷

$$J_{SCLC} = \mu_0 \frac{9}{8} \frac{V^2}{d^3} \varepsilon \varepsilon_0 (0.891 \gamma \sqrt{V/d}) \quad (1)$$

J_{SCLC} is the steady-state current density; μ_0 is the zero field mobility; V is applied voltage; d is the film thickness, ε is the permittivity of the film (~ 3); ε_0 is the vacuum permittivity and γ is the field dependence parameter. The ITO-coated glass substrates had a sheet resistance of 15 Ω/sq and the organic layers were deposited in top of it at a rate $< 0.1 \text{ \AA/s}$, using a MB EcoVap4G vacuum deposition system build in a Kurt J. Lesker glove box. The sample area was of 6 mm². The charge drift mobility of **1** was estimated as previously described from J. C. Blakesley *et al.*⁸ All the theoretic calculations were performed with the software package Gaussian09 (Revision A.02).⁹

Synthesis of dimethyl 4,4'-(benzo[c][1,2,5]thiadiazole-4,7-diyl)bis(3-methoxybenzoate) (**1**)

4,7-Bis(4,4,5,5-tetramethyl-1,3,2-dioxaborolan-2-yl)benzo[c][1,2,5]thiadiazole (100 mg, 0.258 mmol), potassium phosphate (109 mg, 0.515 mmol), [1,1'-bis(diphenylphosphino)ferrocene]-dichloropalladium(II) dichloromethane adduct (21 mg, 0.026 mmol) and methyl 4-iodo-3-methoxybenzoate (226 mg, 0.773 mmol) were charged under nitrogen in a two-neck round-bottom flask. Degassed water (1 mL) and dimethylformamide (9 mL) were added and the mixture was stirred at 60°C for 18 hours. After this time the mixture was diluted with brine (50 mL) and extracted with dichloromethane (3 x 50 mL). The recombined organic layers were washed with brine (2 x 50 mL), water (3 x 50 mL), dried over MgSO₄ and concentrated under reduced pressure to

afford a dark yellow solid. Purification on silica gel, eluting dichloromethane to wash off the impurities and then chloroform afforded a dark yellow powder. The title compound (**1**) was obtained after recrystallisation from hot acetone as a bright yellow powder (69 mg, 58%). TGA: 5% mass loss at 311 °C; $T_m = 227$ °C, $T_c = 147$ °C; ^1H NMR (400.1 MHz, CDCl_3 , δ) 7.81 (dd, $J = 7.8, 1.5$ Hz, 2H, Ar H), 7.77 (d, $J = 1.5$ Hz, 2H, Ar H), 7.76 (s, 2H, Ar H), 7.65 (d, $J = 7.8$ Hz, 2H, ArH), 3.97 (s, 6H, COOCH_3), 3.88 (s, 6H, OCH_3); ^{13}C NMR (100.6 MHz, CDCl_3 , δ) 166.9, 157.2, 154.1, 131.9, 131.5, 131.2, 130.5, 129.9, 122.1, 112.4, 56.1, 52.4; MALDI (m/z (%)) 464.15 (100), 465.12 (75), 466.14 (30); HRMS (LSI-TOF) m/z $[\text{M} + \text{H}]^+$ calcd for $\text{C}_{24}\text{H}_{21}\text{N}_2\text{O}_6\text{S}$ 465.1115, found 465.1117. Melting Point: 230-232 °C.

Table S1. Energies, wavelengths, oscillator strengths, symmetry and orbital assignments of the first 20 singlet vertical electronic transitions for **1** (vacuum) calculated at the PBE0/6-311G(d,p) level of theory.

Energy (eV)	Wavelength λ (nm)	Oscillator Strength	Symmetry	Major contributions
2.99	415.0	0.4026	Singlet	HOMO→LUMO (98%)
3.49	355.3	0.0074	Singlet	H-1→LUMO (99%)
3.74	331.3	0.0267	Singlet	H-2→LUMO (96%)
3.98	311.2	0.6020	Singlet	HOMO→L+1 (95%)
4.12	300.9	0.0058	Singlet	H-3→LUMO (74%), HOMO→L+2 (13%)
4.33	286.1	0.0636	Singlet	H-4→LUMO (25%), HOMO→L+2 (63%)
4.48	276.7	0.0509	Singlet	H-4→LUMO (52%), H-1→L+1 (12%), HOMO→L+2 (10%)
4.55	272.4	0.0443	Singlet	H-1→L+1 (64%), HOMO→L+2 (10%)
4.62	268.6	0.0248	Singlet	H-2→L+1 (50%), H-1→L+2 (31%)
4.73	262.2	0.0178	Singlet	H-5→LUMO (89%)
4.74	261.4	0.0002	Singlet	H-8→LUMO (43%), H-6→LUMO (32%)
4.78	259.3	0.0002	Singlet	H-7→LUMO (63%), H-7→L+1 (14%), H-6→L+2 (17%)
4.81	257.9	0.0000	Singlet	H-8→LUMO (33%), H-7→L+2 (13%), H-6→LUMO (31%), H-6→L+1 (12%)
4.98	249.1	0.0460	Singlet	H-2→L+1 (36%), H-1→L+2 (61%)
5.00	248.0	0.0001	Singlet	H-3→L+1 (11%), H-2→L+2 (59%), H-1→L+1 (17%)
5.05	245.8	0.0027	Singlet	H-11→LUMO (79%)
5.14	241.4	0.0162	Singlet	H-4→L+1 (10%), H-3→L+1 (65%), H-2→L+2 (17%)
5.22	237.6	0.0002	Singlet	H-7→L+2 (25%), H-6→LUMO (36%), H-6→L+1 (32%)
5.32	233.1	0.0057	Singlet	H-7→LUMO (33%), H-7→L+1 (25%), H-6→L+2 (22%)
5.33	232.5	0.0630	Singlet	H-3→L+2 (17%), HOMO→L+4 (58%)

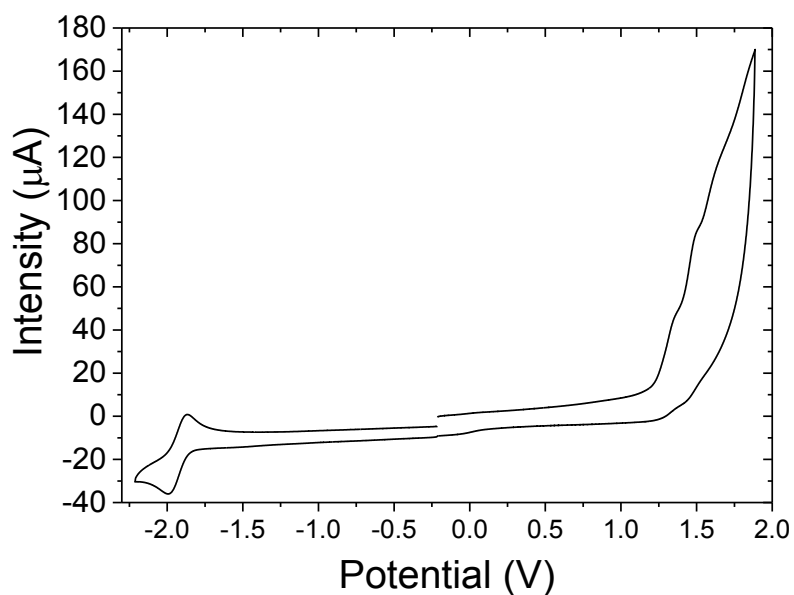


Figure S1. Cyclic voltammogram of **1** ($1 \cdot 10^{-4}$ M solution). Measurements performed using a glassy carbon working electrode, Ag/AgCl reference electrode and platinum wire counter electrode. The supporting electrolyte was 0.1M tetrabutylammonium hexafluorophosphate in dichloromethane. Scan rate of 0.1 Vs^{-1} . All the waves were referenced to ferrocene.

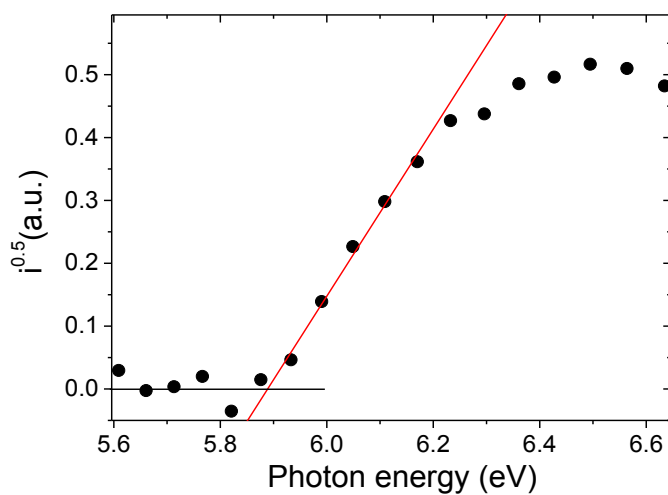


Figure S2. Photoelectron emission spectrum of a thin layer of **1**.

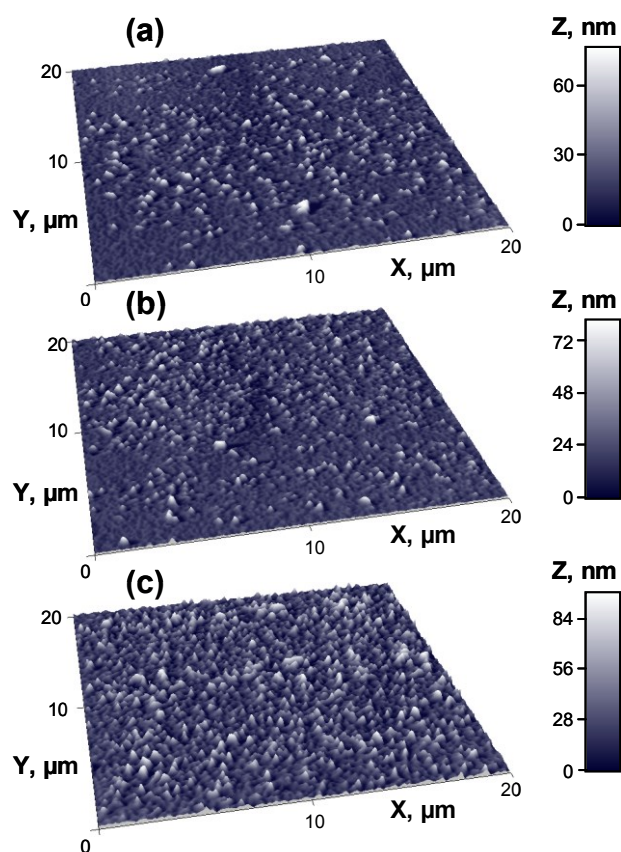


Figure S3. AFM 3D topographical images with normalized Z axis in nm of thin films (30 nm) of **1** prepared by vacuum evaporation at different deposition rates on glass substrates: (a) $<0.1 \text{ \AA/s}$, (b) 1.5 \AA/s and (c) 10 \AA/s . The images were acquired in air using contact mode.

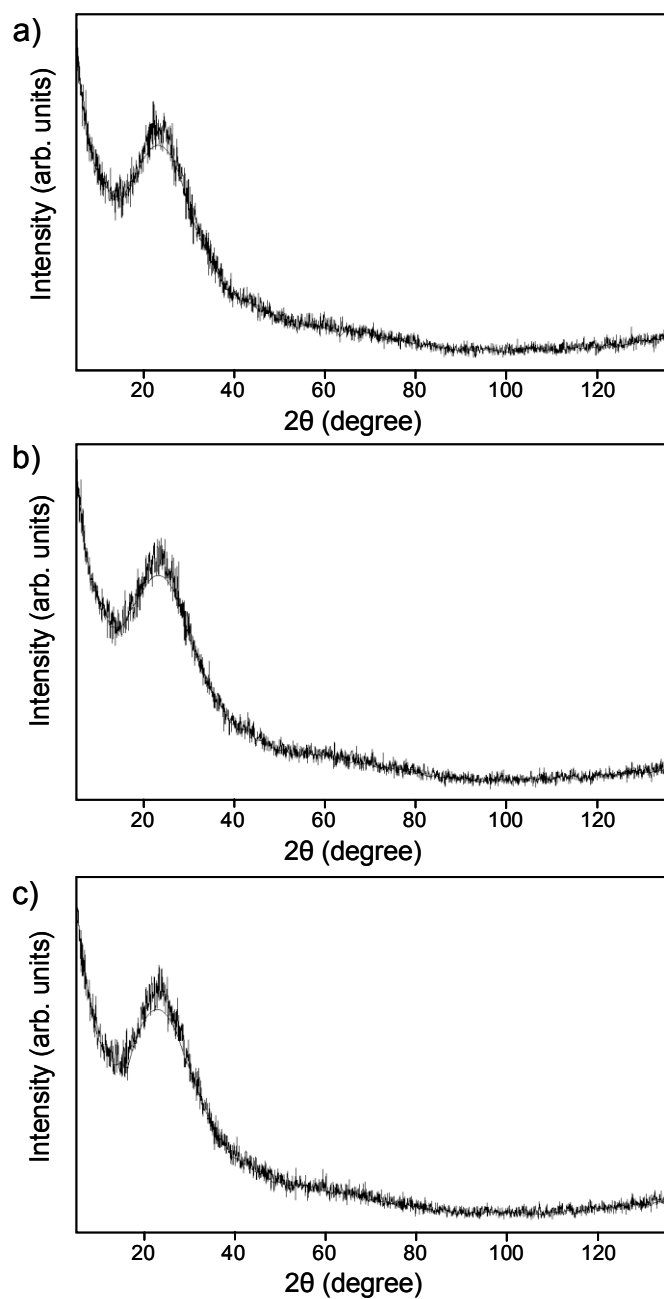


Figure S4. X-ray diffraction patterns a grazing incidence angle of 1.50° of thin films of **1** prepared by vacuum evaporation at different deposition rates on glass substrates: (a) $<0.1 \text{ \AA/s}$, (b) 1.5 \AA/s and (c) 10 \AA/s .

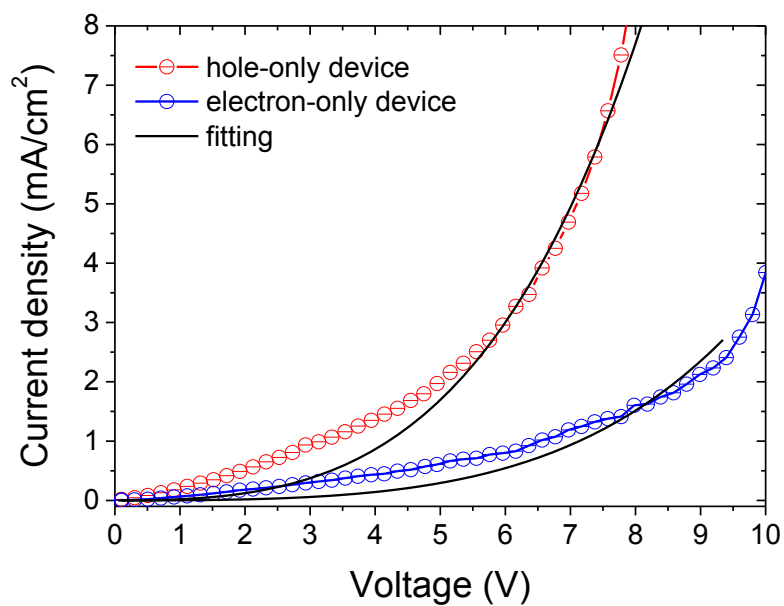


Figure S5 Current density-voltage characteristic curves and fittings of the hole only and electron only devices. The disagreement between the experimental and fit curves can be explained taking in account the existence of electron and hole traps in **1** due to its morphology.

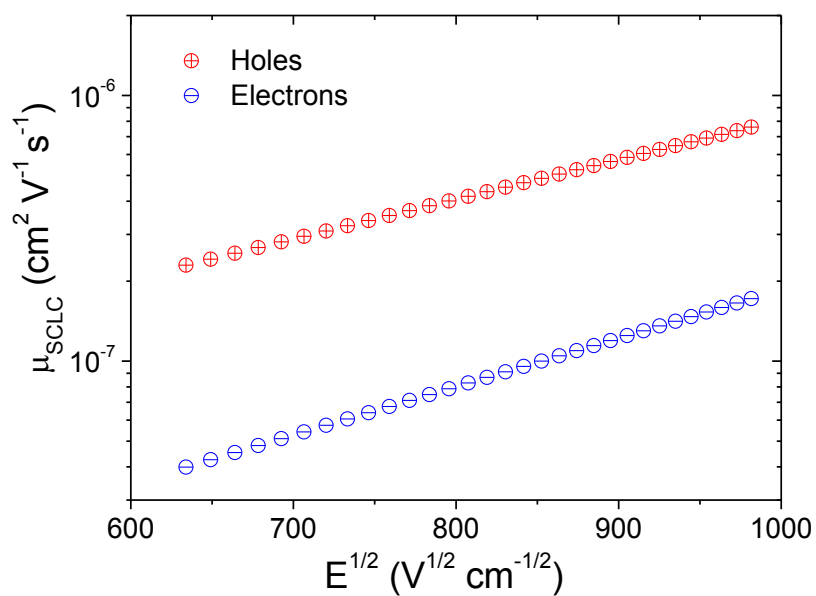


Figure S6 Hole and electron mobility of **1** at different square root of the applied electric field.

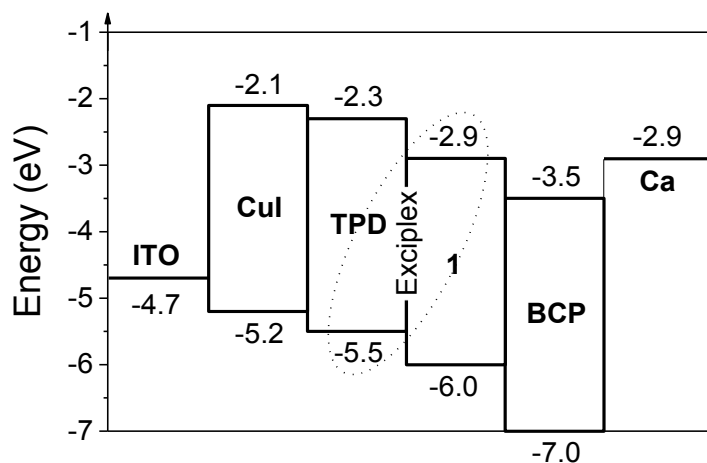


Figure S7. Energy-band diagram of the fabricated device. Aluminium was used on the cathode for the passivation of the calcium electrode, in order to investigate the properties of the device in ambient atmosphere at room temperature immediately after device fabrication.

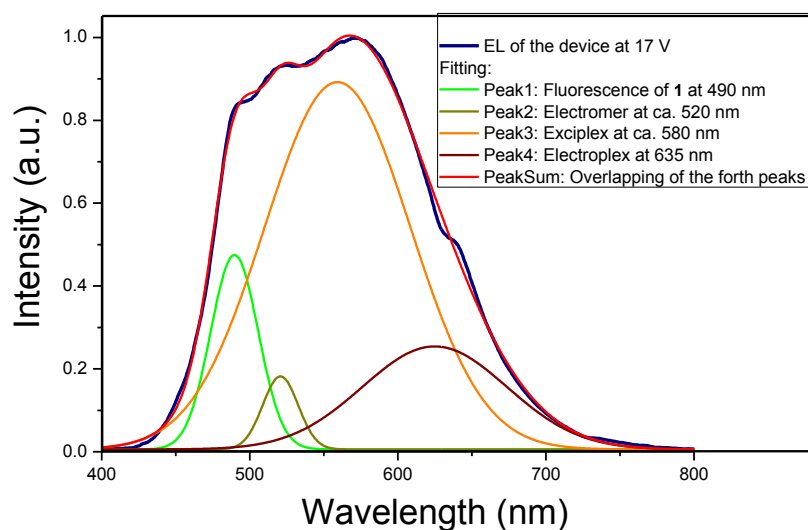


Figure S8. Fitting of the electroluminescence spectrum at 17 V of the OLED, providing the assignments of the different peaks.

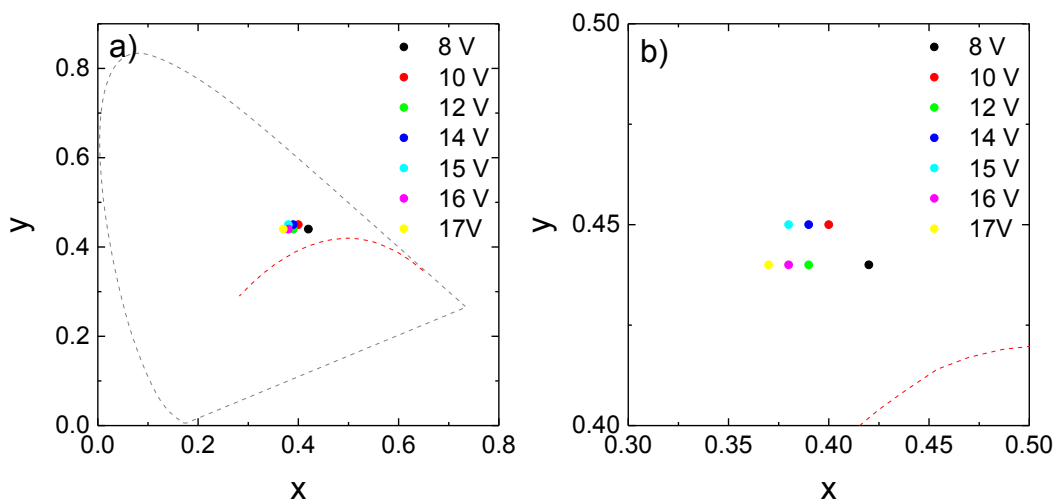


Figure S9 The different colour coordinates of the device under different applied voltages.

Table S2. The different colour coordinates of the device under different applied voltages.

Applied voltage (V)	CIE 1931 coordinates
8	(0.42, 0.44)
10	(0.40, 0.45)
12	(0.39, 0.44)
14	(0.39, 0.45)
15	(0.38, 0.45)
16	(0.38, 0.44)
17	(0.37, 0.44)

Table S3. Summary of the characteristics of the device.

V_{on} at 1.4 Cd/m ² (V)	Max Brightness (cd/m ²)	Max current efficiency (cd/A)	Max power Efficiency (lm/W)	Max external Quantum efficiency (%)	CIE 1931 Coordinates (x, y)	Colour Temperature (K)
5.8	5219	6.5	2.6	2.39	(0.39, 0.44)	4500

Table S4. Current efficiency, power efficiency and external quantum efficiency of the device at different current densities and brightness.

Current density	Current efficiency (cd/A)	Power efficiency (lm/W)	External quantum efficiency (%)
10 mA/cm ²	6.23	1.96	2.3
100 mA/cm ²	3.99	2.57	1.47
Brightness			
100 Cd/m ²	6.55	0.96	2.42
1000 Cd/m ²	5.31	1.54	1.96

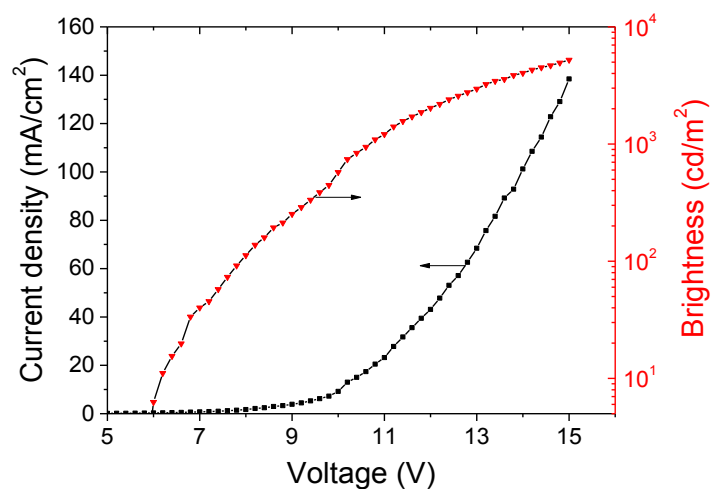


Figure S10. Current density–voltage and luminance–voltage characteristics of the device.

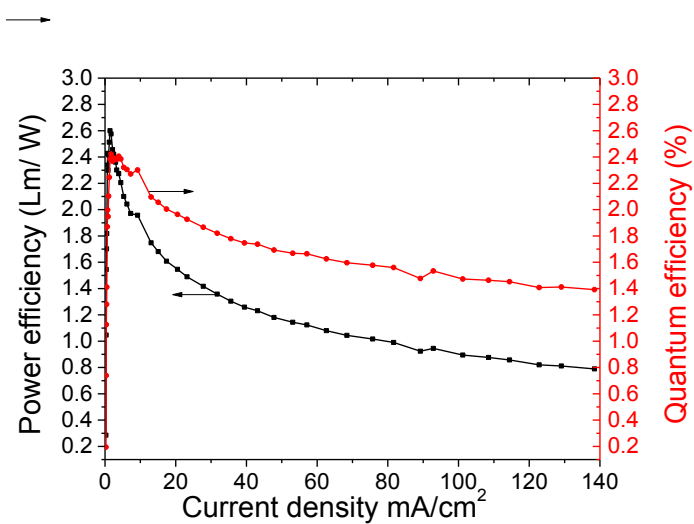


Figure S81. Power efficiency and external quantum efficiency of the device.

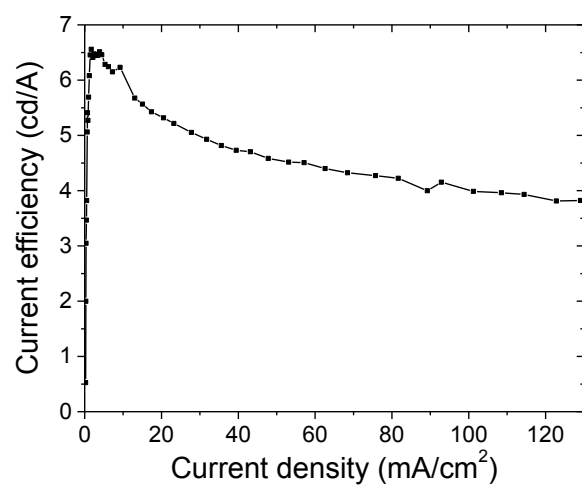


Figure S12. Current efficiency–current density characteristic of the device.

Table S5. Mean signed and mean square errors (MSiE and MSqE, eV) and maximal deviations (Max-Min, eV), obtained by comparing experimental and theoretical mean maximum absorption values of literature compound 4,7-dithiophenyl-benzothiadiazole (**3**).¹⁰ Using the TD-DFT method including the polarisable continuum model (PCM)¹¹ (dichloromethane) the vertical transitions were calculated for **3**, using the combination of five different functionals (B3LYP¹², wB97xD,¹³ CAM-B3LYP,¹⁴ M06-2X,¹⁵ PBE0)¹⁶ and three different basis sets (6-31G, 6-311G(d,p), 6-311+G(2d,p), DGDZVP). Six vertical absorptions were simulated at each level of theory and they were fitted with Gaussian curves (full width at half maximum (FWHM) = 0.37 eV) using the software GaussSum 3.0.¹⁷ The two maxima obtained with this procedure were compared with the experimental maxima absorption bands of **3**. The level of theory PBE0/6-311G(d,p) have shown the smallest mean signed and mean square errors (the smallest shift of the vertical absorptions calculated in comparison with the experimental data) and it was used for all further calculations.

	B3LYP				wB97X-D			
	6-31G	6-311G(d,p)	6-311+G(2d,p)	DGDZVP	6-31G	6-311G(d,p)	6-311+G(2d,p)	DGDZVP
MSiE	-0.323	-0.281	-0.319	-0.397	0.463	0.475	0.436	0.436
MSqE	0.113	0.087	0.109	0.166	0.231	0.241	0.199	0.202
Max(+)	-0.228	-0.190	-0.236	-0.306	0.593	0.601	0.531	0.546
Min(-)	-0.418	-0.372	-0.402	-0.488	0.334	0.349	0.341	0.326

	CAM-B3LYP				M06-2X			
	6-31G	6-311G(d,p)	6-311+G(2d,p)	DGDZVP	6-31G	6-311G(d,p)	6-311+G(2d,p)	DGDZVP
MSiE	0.363	0.405	0.359	0.316	0.363	0.421	0.351	0.335
MSqE	0.155	0.182	0.139	0.117	0.160	0.197	0.134	0.130
Max(+)	0.515	0.539	0.461	0.446	0.531	0.562	0.453	0.469
Min(-)	0.210	0.272	0.256	0.186	0.194	0.279	0.248	0.202

	PBE0			
	6-31G	6-311G(d,p)	6-311+G(2d,p)	DGDZVP
MSiE	-0.153	-0.114	-0.153	-0.153
MSqE	0.037	0.025	0.032	0.034
ax(+)	-0.035	-0.004	-0.058	-0.050
Min(-)	-0.271	-0.224	-0.248	-0.255

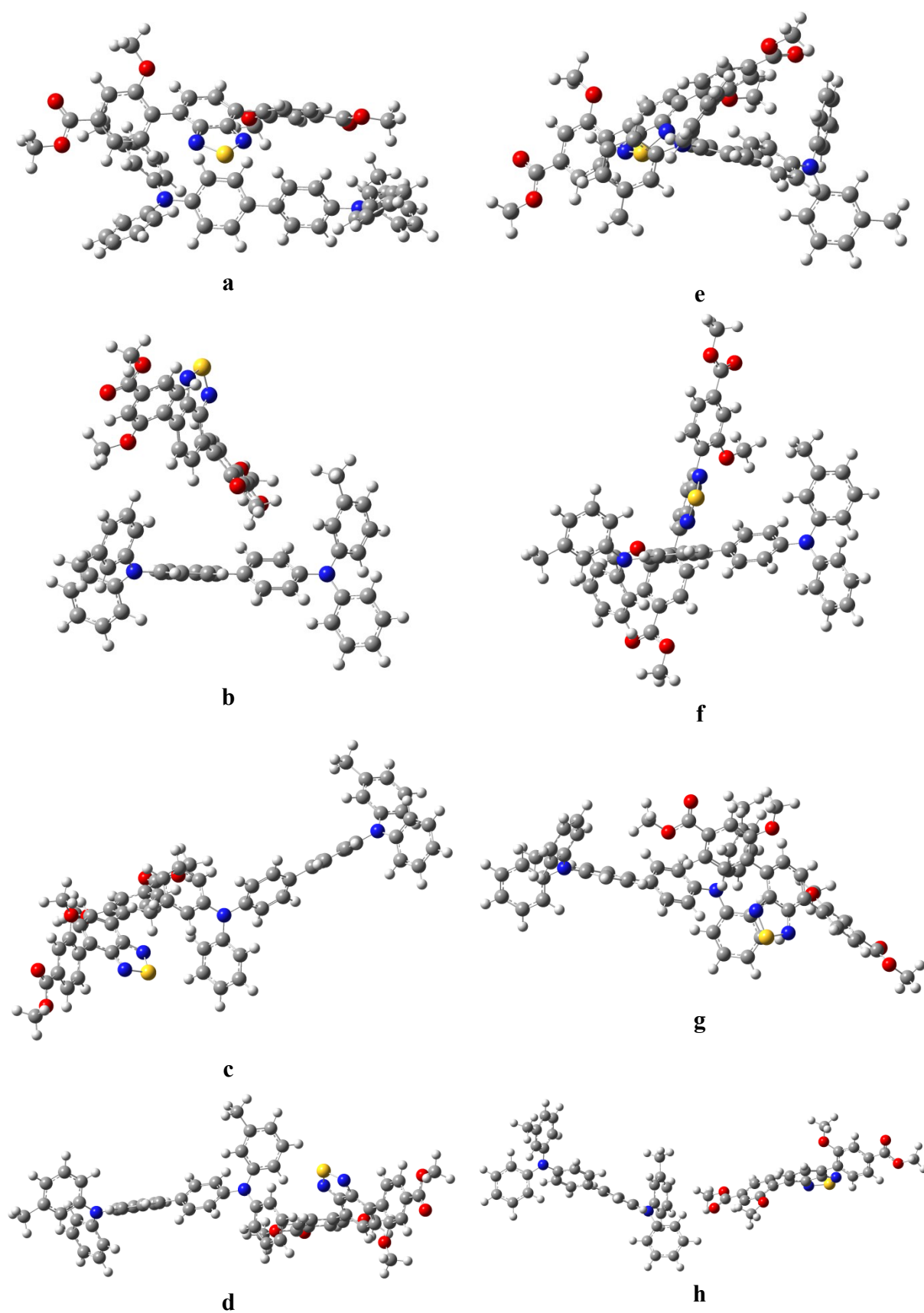


Figure S9. Optimised geometries for height different TPD:1 complexes (a-h), calculated at the PBE0/6-311G(d,p) level of theory.

Table S6. Relative total energies for height different **TPD:1** complexes (**a-h**), calculated at the PBE0/6-311G(d,p) level of theory.

Complex	Relative total energy (kcal/mol)
a	0.00
b	2.42
c	2.97
d	3.40
e	1.30
f	3.95
g	1.92
h	3.29

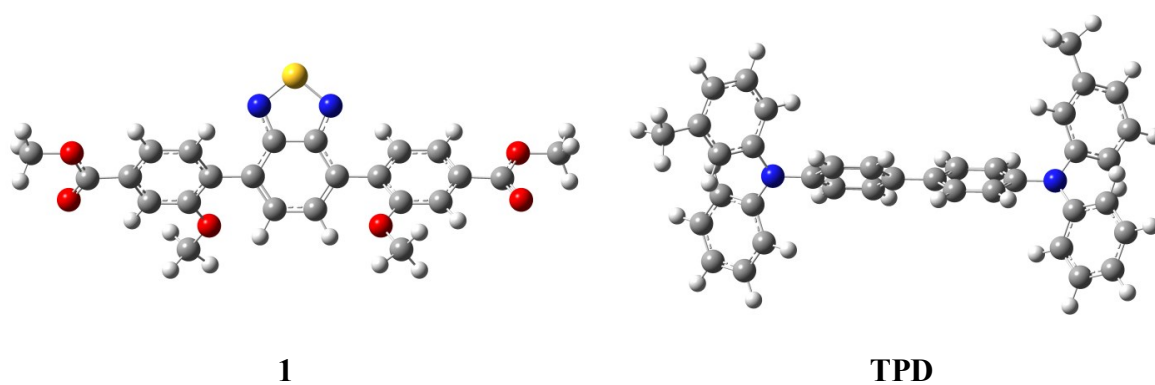


Figure S14. Optimised geometries of **1** and **TPD** calculated at the PBE0/6-311G(d,p) level of theory.

Table S7. Energies, wavelengths, oscillator strengths, symmetry and orbital assignments of the first 20 singlet vertical electronic transitions for **TPD** (vacuum) calculated at the PBE0/6-311G(d,p) level of theory.

Energy (eV)	Wavelength (nm)	Oscillator Strength	Symmetry	Major contributions
3.48	356.0	1.0686	Singlet	HOMO->LUMO (96%)
3.78	328.0	0.0097	Singlet	H-1->L+2 (14%), HOMO->L+1 (83%)
3.84	323.3	0.0191	Singlet	H-1->L+1 (21%), HOMO->L+2 (75%)
3.95	313.8	0.0005	Singlet	H-1->LUMO (95%)
4.03	307.5	0.1855	Singlet	H-1->L+3 (17%), HOMO->L+3 (78%)
4.05	306.2	0.1792	Singlet	H-1->L+4 (16%), HOMO->L+4 (80%)
4.36	284.5	0.0661	Singlet	H-1->L+2 (27%), HOMO->L+6 (56%)
4.42	280.7	0.0005	Singlet	H-1->L+1 (72%), HOMO->L+2 (19%)
4.46	277.8	0.0009	Singlet	HOMO->L+5 (52%), HOMO->L+8 (13%)
4.48	277.0	0.0182	Singlet	H-1->L+6 (15%), HOMO->L+7 (43%), HOMO->L+8 (11%), HOMO->L+9 (10%)
4.51	275.1	0.0366	Singlet	H-1->L+8 (13%), HOMO->L+7 (21%), HOMO->L+9 (42%)
4.53	274.0	0.0041	Singlet	H-1->L+2 (49%), HOMO->L+1 (11%), HOMO->L+6 (23%)
4.59	270.3	0.0002	Singlet	HOMO->L+5 (35%), HOMO->L+8 (43%)
4.64	267.5	0.0403	Singlet	H-1->L+3 (79%), HOMO->L+3 (18%)
4.65	266.5	0.0387	Singlet	H-1->L+4 (81%), HOMO->L+4 (17%)
4.67	265.7	0.0262	Singlet	H-1->L+5 (83%)
4.69	264.4	0.0014	Singlet	H-1->L+6 (74%), HOMO->L+9 (11%)
4.70	263.6	0.0058	Singlet	H-1->L+7 (31%), H-1->L+9 (43%), HOMO->L+6 (13%)
4.80	258.2	0.0201	Singlet	H-2->LUMO (16%), H-1->L+8 (38%), HOMO->L+7 (11%), HOMO->L+10 (13%)
4.85	255.8	0.0001	Singlet	H-1->L+7 (39%), H-1->L+9 (20%), HOMO->L+8 (22%)

Table S8. Energies, wavelengths, oscillator strengths, symmetry and orbital assignments of the first 20 singlet vertical electronic transitions for the complex **TPD:1** (vacuum) calculated at the PBE0/6-311G(d,p) level of theory. It is assumed that emission can be generated from all the excited state energy levels.

Energy (eV)	Wavelength (nm)	Oscillator Strength	Symmetry	Major contributions
2.06	600.7	0.0001	Singlet	HOMO->LUMO (95%)
2.44	508.7	0.0000	Singlet	H-1->LUMO (94%)
2.99	414.0	0.3039	Singlet	H-2->LUMO (98%)
3.09	401.7	0.0010	Singlet	HOMO->L+1 (95%)
3.33	372.9	0.0020	Singlet	H-1->L+1 (30%), HOMO->L+2 (67%)
3.49	355.1	0.0199	Singlet	H-4->LUMO (48%), H-3->LUMO (48%)
3.51	353.3	0.0006	Singlet	H-1->L+1 (65%), HOMO->L+2 (25%)
3.54	350.3	0.7465	Singlet	HOMO->L+3 (93%)
3.70	335.2	0.0080	Singlet	H-5->LUMO (10%), H-4->LUMO (34%), H-3->LUMO (34%)
3.74	331.8	0.0142	Singlet	H-7->LUMO (36%), H-1->L+2 (52%)
3.74	331.5	0.0215	Singlet	H-7->LUMO (40%), H-1->L+2 (30%)
3.75	330.6	0.0042	Singlet	H-6->LUMO (23%), H-5->LUMO (45%), HOMO->L+4 (12%)
3.78	328.4	0.0123	Singlet	H-1->L+4 (18%), HOMO->L+4 (53%)
3.81	325.4	0.0265	Singlet	H-1->L+5 (13%), HOMO->L+5 (74%)
3.82	324.8	0.0061	Singlet	H-1->L+3 (83%)
3.83	324.1	0.0016	Singlet	H-9->LUMO (26%), H-6->LUMO (28%), H-5->LUMO (24%)
3.86	321.0	0.5182	Singlet	H-2->L+1 (87%)
3.90	318.1	0.0003	Singlet	H-8->LUMO (80%)
3.94	314.9	0.0006	Singlet	H-9->LUMO (51%), H-6->LUMO (28%)
3.96	313.2	0.1328	Singlet	H-1->L+6 (23%), HOMO->L+6 (66%)

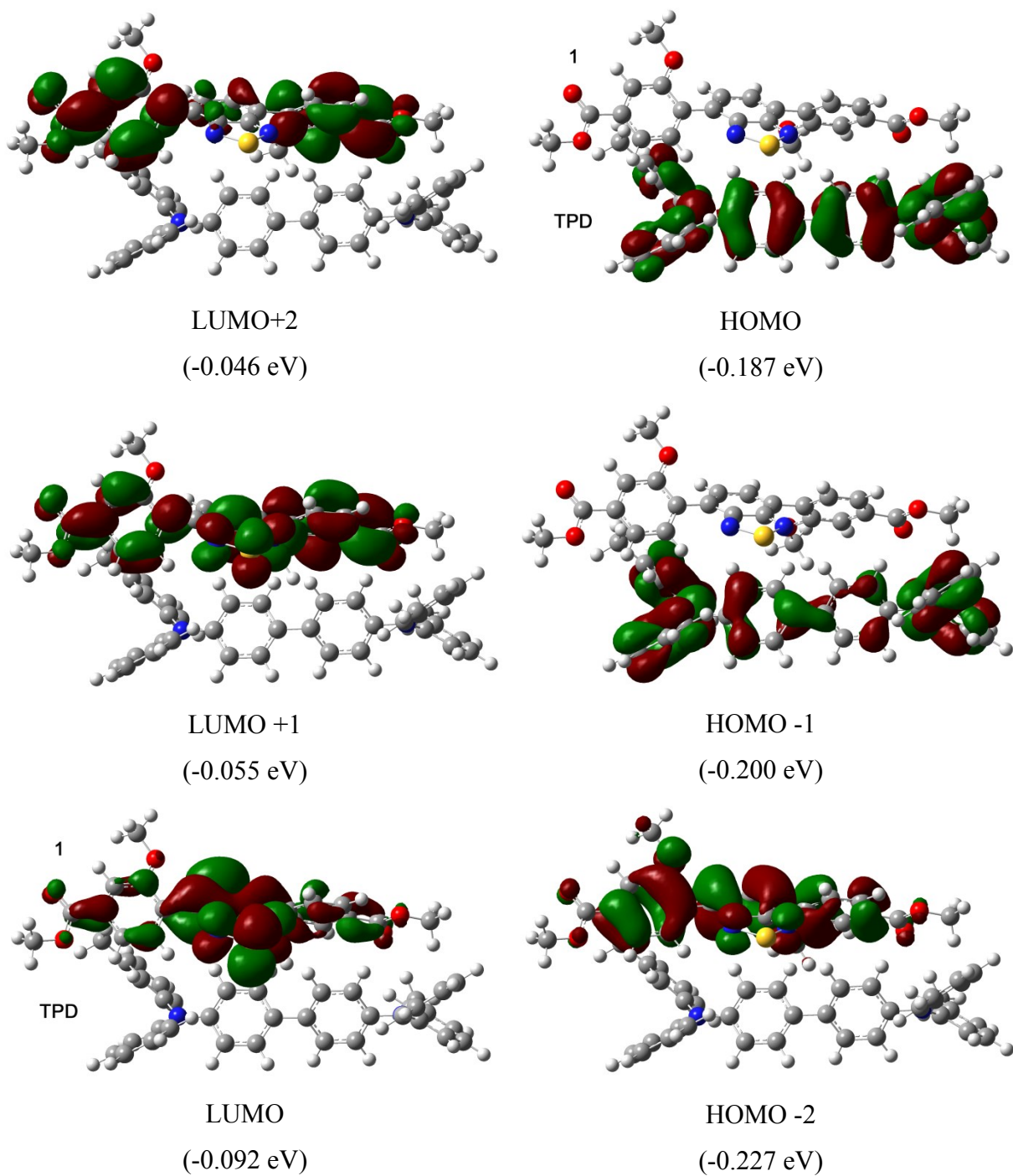


Figure S15. Molecular orbital graphical representations and energies (HOMO-2 to LUMO+2) of the **TPD:1** complex calculated at the PBE0/6-311G(d,p) level of theory (isosurface 0.02).

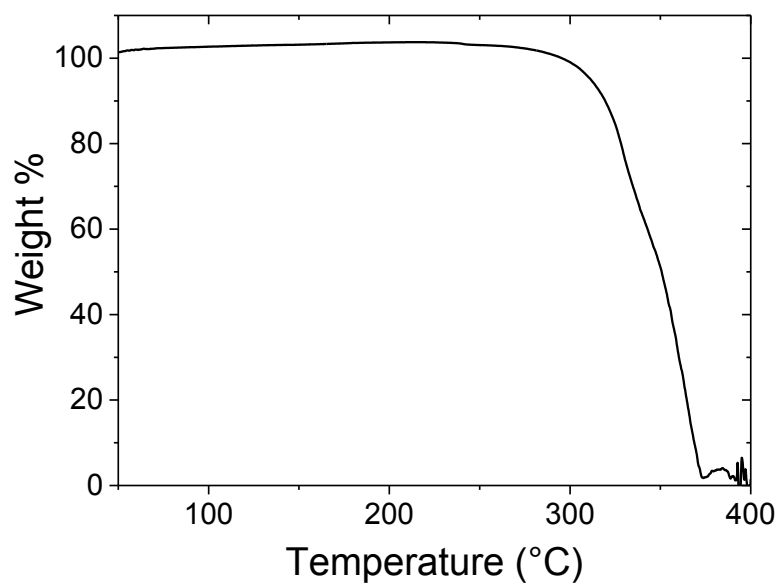


Figure S16. Thermogravimetric analyses of **1** in Argon (40-450°C). The small increment in the mass of the sample that is observed between 50 and 250°C is likely due to the Archimede's effect. When the object is under a current of fluid (nitrogen), the fluid tends to force the object upwards. When the analyser was tared the fluid (N₂) likely forced the sample upwards. In this way when the analysis starts, the density of the fluid was slightly decreased (by increasing the temperature) and consequently the hanged sample goes down. Then when these changes where recorded a mass increment is shown, produced by a small change in the density of the surrounding fluid. This effect is worse at higher heating rates.

D211974.1.fid — Person 7-16 — EA033_copy — @proton CDCl3 {C:\NMRdata} pjs 30

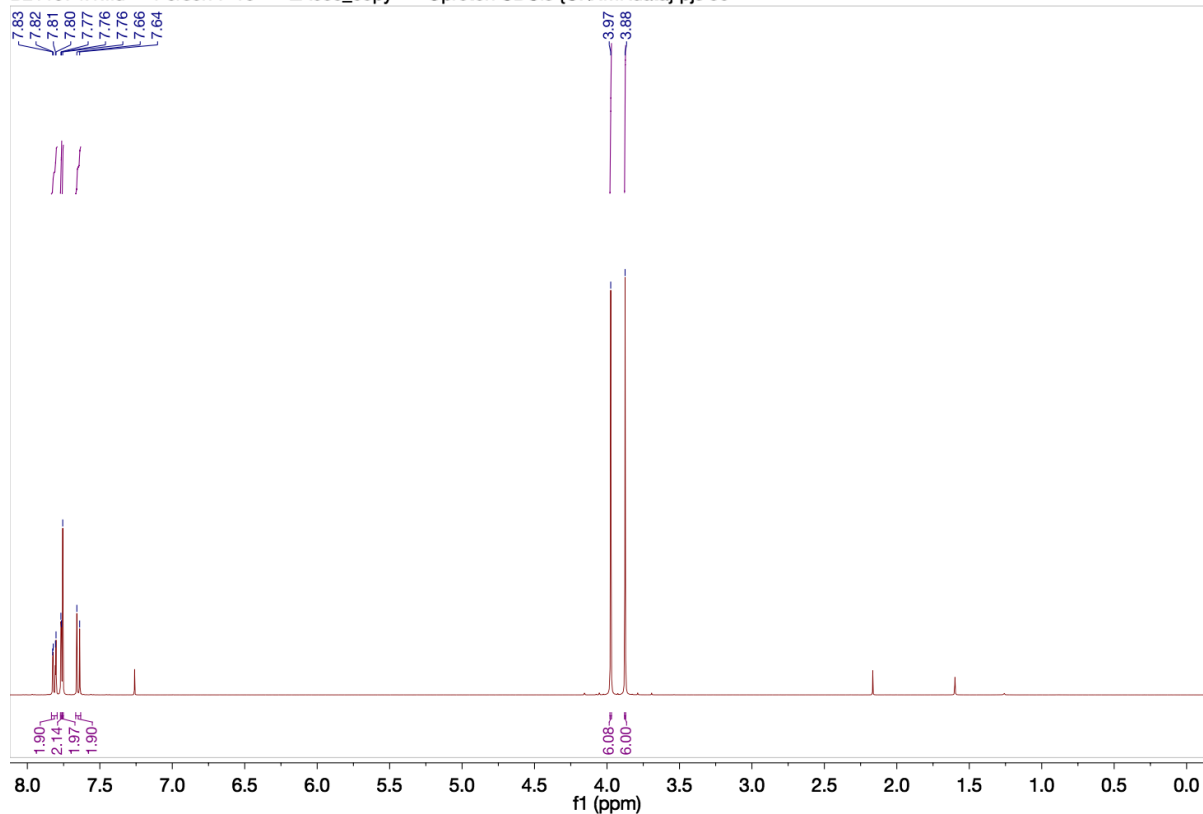


Figure S17. ¹H NMR spectrum of **1** recorded in deuterated chloroform.

D211974.2.fid — Person 7-16 — EA033_copy — ¹³C_@ CDCl3 {C:\NMRdata} pjs 30

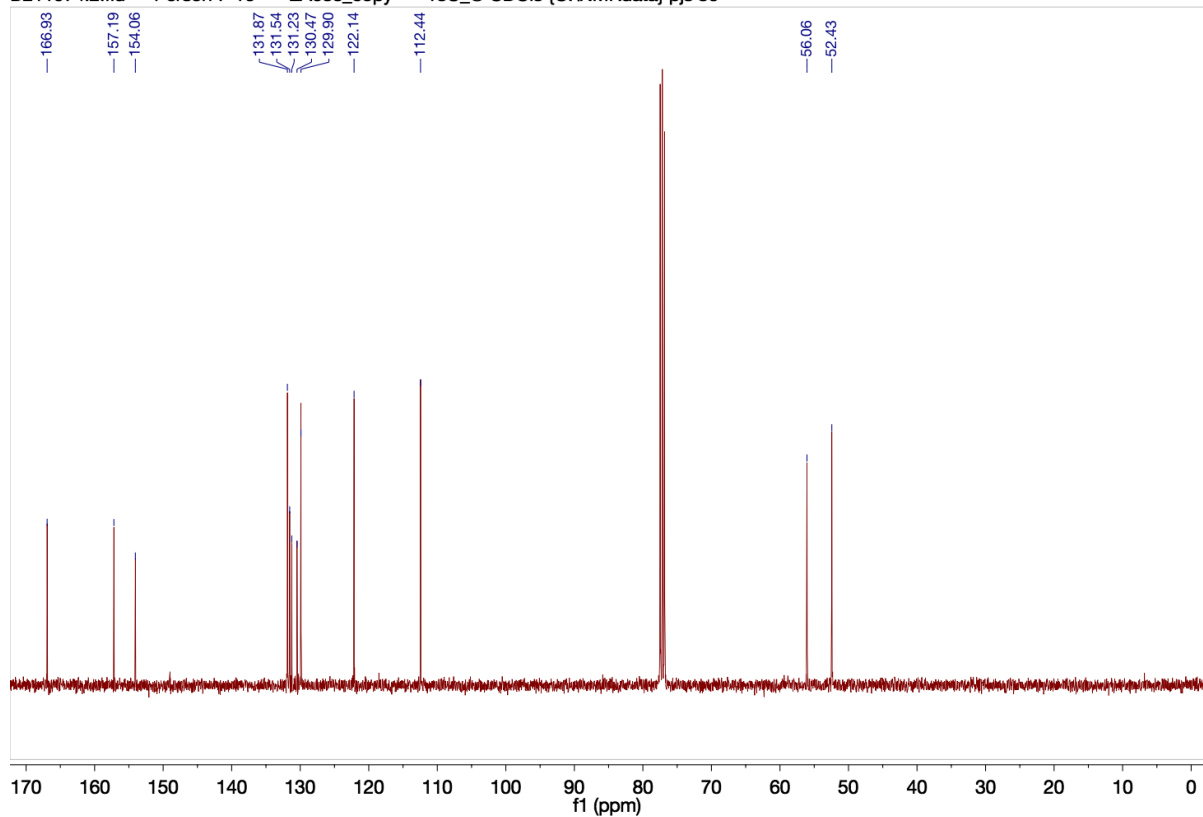


Figure S18. ¹³C NMR spectrum of **1** recorded in deuterated chloroform.

References

- 1 D. Rankine, A. Avellaneda, M. R. Hill, C. J. Doonan, C. J. Sumby, *Chem. Commun.*, **2012**, 48, 10328.
- 2 J. C. de Mello, H. F. Wittmann, R. H. Friend, *Adv. Mater.*, **1997**, 9, 230.
- 3 E. Miyamoto, Y. Yamaguchi, M. Yokoyama, *J. Imaging Sci. Technol.*, **1989**, 28, 364.
- 4 V. Cherpak, A. Gassmann, P. Stakhira, D. Volyniuk, J. V. Grazulevicius, A. Michaleviciute, A. Tomkeviciene, G. Barylo, H. von Seggern, *Org. Electron.*, **2014**, 15, 1396.
- 5 N. C. Greenham, R. H. Friend, D. D. C. Bradley, *Adv. Mater.*, **1994**, 6, 491.
- 6 M. A. F. Baldo, S. R.; Thompson, M. E. , *Organic Electroluminescence*, CRC Press, 2005.
- 7 N. F. Mott, R. W. Gurney, *Electronic Processes in Ionic Crystals*, Oxford, 1940.
- 8 J. C. Blakesley, F. A. Castro, W. Kylberg, G. F. A. Dibb, C. Arantes, R. Valaski, M. Cremona, J. S. Kim, J.-S. Kim, *Org. Electron.*, **2014**, 15, 1263.
- 9 M. J. Frisch, G. W. Trucks, H. B. Schlegel, G. E. Scuseria, M. A. Robb, J. R. Cheeseman, G. Scalmani, V. Barone, B. Mennucci, G. A. Petersson, H. Nakatsuji, M. Caricato, X. Li, H. P. Hratchian, A. F. Izmaylov, J. Bloino, G. Zheng, J. L. Sonnenberg, M. Hada, M. Ehara, K. Toyota, R. Fukuda, J. Hasegawa, M. Ishida, T. Nakajima, Y. Honda, O. Kitao, H. Nakai, T. Vreven, J. A. Montgomery Jr., J. E. Peralta, F. Ogliaro, M. J. Bearpark, J. Heyd, E. N. Brothers, K. N. Kudin, V. N. Staroverov, R. Kobayashi, J. Normand, K. Raghavachari, A. P. Rendell, J. C. Burant, S. S. Iyengar, J. Tomasi, M. Cossi, N. Rega, N. J. Millam, M. Klene, J. E. Knox, J. B. Cross, V. Bakken, C. Adamo, J. Jaramillo, R. Gomperts, R. E. Stratmann, O. Yazyev, A. J. Austin, R. Cammi, C. Pomelli, J. W. Ochterski, R. L. Martin, K. Morokuma, V. G. Zakrzewski, G. A. Voth, P. Salvador, J. J. Dannenberg, S. Dapprich, A. D. Daniels, Ö. Farkas, J. B. Foresman, J. V. Ortiz, J. Cioslowski, D. J. Fox, *Gaussian 09*, **2009**.
- 10 S.-i. Kato, T. Matsumoto, T. Ishi-i, T. Thiemann, M. Shigeiwa, H. Gorohmaru, S. Maeda, Y. Yamashita, S. Mataka, *Chem. Commun.*, **2004**, 2342.
- 11 S. Miertuš, E. Scrocco, J. Tomasi, *Chem. Phys.*, **1981**, 55, 117.
- 12 A. D. Becke, *J. Chem. Phys.*, **1993**, 98, 5648.
- 13 J.-D. Chai, M. Head-Gordon, *Phys. Chem. Chem. Phys.*, **2008**, 10, 6615.
- 14 T. Yanai, D. P. Tew, N. C. Handy, *Chem. Phys. Lett.*, **2004**, 393, 51.
- 15 Y. Zhao, D. Truhlar, *Theor. Chem. Acc.*, **2008**, 120, 215.
- 16 C. Adamo, V. Barone, *J. Chem. Phys.*, **1999**, 110, 6158.
- 17 N. M. O'Boyle, A. L. Tenderholt, K. M. Langner, *J. Comput. Chem.*, **2008**, 29, 839.